SIGNAL ENHANCEMENT AND GEOMETRIC INFORMATION RETRIEVAL FROM 2-D GPR DATA WITH MULTISCALE, ORIENTATION-SENSITIVE FILTERING METHODS

Andreas Tzanis

Department of Geophysics and Geothermy,
National and Kapodistrian University of Athens,
Panepistimiopoli,
Zografou 15784,Greece.
E-mail: atzanis@geol.uoa.gr

Modified version of paper published in:

First Break, Vol. 32, No 8, pp. 91-98, August 2014.

Athens, August 2014

Abstract

The Ground Probing Radar (GPR) is a valuable tool for near surface geological, geotechnical, engineering, environmental, archaeological and other work. GPR data frequently contain anisotropic geometric information from various structures such as bedding, cracks, fractures etc. Such features are generally recorded as wavefronts and are frequently the target of a survey. However, they are usually not good reflectors and they are highly localized in time and in space. Their scale is therefore a factor significantly affecting detectability. At the same time, GPR is sensitive to broadband noise from buried small objects, electromagnetic anthropogenic activity and systemic factors, which frequently obscures reflections from such targets. This presentation discusses the case of de-noising GPR data and retrieving geometric information with advanced scale-and-orientation-sensitive filtering methods. These include orthogonal steerable wavelet arrays and the Gabor wavelet in particular, as well as multiscale/multidirectional optimally sparse representations of bivariate functions with singularities on curves, the archetypal example of the latter being the Curvelet Transform. This approach to processing is demonstrated with examples to be exceptionally adaptive and highly effective. It is also not limited to GPR data.

1 Introduction

The Ground Probing Radar (GPR) is an almost indispensable means of imaging near surface structures and enjoys a very diverse and broad range of applications. Two-dimensional GPR images of the subsurface frequently contain geometric information from small scatterers (diffraction hyperbolae) as well as dip-dependent information from dipping reflectors such as geological bedding, structural interfaces, cracks, fractures, joints, empty or filled cavities associated with jointing or faulting and other conceivable structural configuration. The second group of targets, especially fractures, are usually not good reflectors and are spatially localized; in geological, geotechnical and engineering applications their detection is frequently a primary objective. At the same time, GPR is notoriously susceptible to noise. An innumerable variety of natural and artificial buried objects can cause unwanted reflections and scattering. Anthropogenic noise is worse and includes reflections from nearby structures, interference from power lines and telecommunication devices etc. This type of noise is only partially countered with shielded antennae while the extraneous or reflected airwaves, critically refracted airwaves and groundwaves are not easily suppressed during acquisition. Finally, there's systemic noise, frequently manifested as ringing (antenna self-clutter). In many cases, the noise has definite geometrical characteristics (e.g. high-angle crossing clutter). Because the GPR source wavelet is tuned at a single frequency, the information returned by the subsurface structure is usually limited to a relatively narrow band around it and the rest of the spectrum is swamped in noise. Raw GPR data usually require post-acquisition processing, as they provide only approximate target shapes and depths.

This presentation will introduce and demonstrate the application of advanced filtering methods of information retrieval to GPR data, with emphasis on recovering features associated with specific spatial or temporal scales and geometry (dip). The requirement to manipulate geometrical (dip-dependent) information limits the methods suitable for this purpose to two general categories: Directional Filters (or Directional Wavelets) and multi-directional Multi-Resolution Analysis (MRA).

Directional Filters are a relatively diverse group, for which an almost complete recount exists in Jacques et al. (2011). The more advanced designs generally comprise anisotropic 2-D waveforms based on steerable semi-orthogonal or orthogonal wavelet arrays, whose frequency and/or wavenumber localization can be manipulated by changing their scale (wavelength) and orientation (dip); this way, directional filters can be tuned at any resolvable trait of the data. The present will focus on tuneable orthogonal Gabor wavelets (e.g.

Feichtinger and Strohmer, 1998, 2003) which have been applied to the analysis GPR data and shown to be very effective (Tzanis, 2013).

Multi-Resolution Analysis (e.g. Chui, 1992; Mallat, 1999) is the design method of most of the practically relevant discrete wavelet transforms and the justification of the fast wavelet transform. MRA allows an image, to be decomposed into a sequence of nested (sub)images arranged in order of increasing detail (decreasing scale), so as to satisfy certain self-similarity relations in time/space, as well as completeness and regularity relations. This provides a means to manipulate localized events but leave the rest of the data generally unaffected. MRA has been applied to GPR data fairly recently, with most of the relevant studies focusing on noise suppression in a time-frequency sense.

Remarkably, the wavelet-based MRA is not efficient in processing geometrical information: just as Fourier methods are not suitable for the analysis of aperiodic phenomena, (which led to the wavelet transform), wavelets are isotropic and unsuitable for application to anisotropic phenomena, as for instance are wavefronts. This problem has been addressed by advanced MRA-like algorithms that are collectively referred to as the "*X-let Transform*" (for a comprehensive review see Jacques et al. (2011). One very effective and versatile approach is the 2nd generation *Curvelet Transform* (Candès and Donoho, 2003a; 2003b; 2004), which is specifically designed to associate scale with orientation. It comprises a multiscale and multidirectional expansion that formulates an optimally sparse representation of objects with edges (specifically of objects which are smooth except for discontinuities along general curves with bounded curvature). The CT traces its origin in Harmonic Analysis, where curvelets were introduced as expansions for asymptotic solutions of wave equations (Smith, 1998; Candès, 1999). In consequence, curvelets can be viewed as primitive and prototype waveforms – they are local in time/space and highly anisotropic, therefore well adapted to detect wavefronts at different angles and scales because curvelets at a given scale can only locally correlate with aligned wavefronts of the same scale. A welcome consequence of optimal sparsity is optimal image reconstruction in case of severely ill-posed problems: one can recover curved objects from noisy data by curvelet shrinkage (analogous to wavelet shrinkage) and obtain a mean squared error that is far better than what was affordable with more traditional methods (Candés et al. 2006).

The main body of the presentation is organized as follows: Succinct introductions of Gabor wavelet filters and the 2nd Generation CT will be given in Sections 2 and 3 respectively. This will be followed by example applications to data featuring straight and curved reflections in complex propagation media and to data contaminated by high levels of noise (Section 4). A brief recapitulation and discussion of the results will conclude the presentation.

2 Gabor Wavelet Filter

In GPR data, the existence of two independent variables (time/ space) allows each component of the f-k spectrum to be coupled with a particular orientation (dip). Thus, it is feasible to design a matrix filter (operator) in which the temporal and/or spatial scale and dip can be varied and tuned at any trait in the data. A Gabor Filter is a Gaussian kernel function modulated by a sinusoidal plane wave. Its impulse response is defined by a harmonic function multiplied by a Gaussian function (Gabor function). The filter has a real and an imaginary component which may be used in combination or individually. The parameterization adopted herein follows the work of Daugman (1985) as further developed by Kruizinga and Petkov (1999) and Grigorescu et al (2002):

$$\mathbf{g}(x,t;\lambda,\theta,\psi,\sigma,\gamma)=\exp\left(-\frac{(x^{\theta})^2+\gamma^2(t^{\theta})^2}{2\sigma^2}\right)\exp\left(j\left(2\pi\frac{x^{\theta}}{\lambda}+\psi\right)\right)$$

where

$$x^{\theta}=x\cos\theta+t\sin\theta$$

$$t^{\theta}=-x\sin\theta+t\cos\theta\ .$$

The parameter λ represents the wavelength of the sinusoidal factor, θ the orientation of the normal to the parallel stripes of a Gabor function, ψ the phase offset, σ the standard deviation of the Gaussian factor and γ the spatial aspect ratio which specifies the ellipticity of the support of the Gabor function. For γ=1 the support is circular; contracting (dilating) γ contracts (dilates) the support in the direction normal to the parallel stripes of the Gabor function. The half-response spectral bandwidth b of a Gabor Filter (in octaves) is related to the ratio σ/λ as follows:

$$b = \log_2\left(\frac{\frac{\sigma}{\lambda}\pi + \sqrt{\frac{\ln 2}{2}}}{\frac{\sigma}{\lambda}\pi - \sqrt{\frac{\ln 2}{2}}}\right), \qquad \frac{\sigma}{\lambda} = \frac{1}{\pi}\sqrt{\frac{\ln 2}{2}} \cdot \frac{2^b + 1}{2^b - 1}$$

Thus, the value of σ may not be specified directly and may be set through the more intuitive parameter b. The smaller the bandwidth, the larger is σ, the support of the Gabor function and the number of visible parallel excitatory and inhibitory stripe zones.

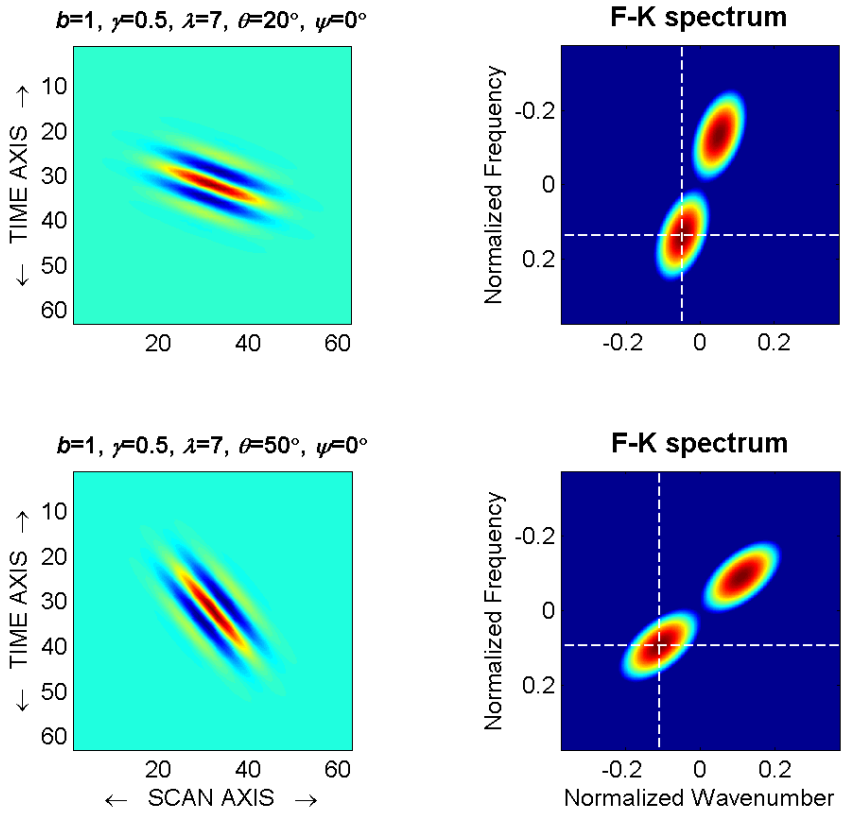

Figure 1. The real part of a Gabor wavelet filter (impulse response) at different orientations. The time axis (t) corresponds to θ=0° and the space axis (x) to θ=90°. To isolate dipping reflectors the filter must be rotated so that the sinusoidal parallel excitatory and inhibitory stripe zones are aligned with the reflector. The f-k spectrum comprises two lobes symmetric with respect to the origin, which rotate *identically* with the impulse response and whose peak coordinates are controlled by the wavelength and the orientation.

The f-k spectrum of the Gabor wavelet rotates identically with its t-x counterpart and is (e.g. Tzanis, 2013)

$$\mathbf{G}(f^\theta, k^\theta) = \frac{4\pi^2\sigma^2}{\gamma}\exp\left(-2\pi^2\sigma^2\left[(k^\theta)^2 + \frac{(f^\theta)^2}{\gamma^2}\right]\right)\cdot\exp(i\psi)\,.$$

It consists of two lobes symmetric with respect to the origin. The location of the peak of the lobes with respect to the frequency (f^θ) and wavenumber axis (k^θ) axes is determined by the wavelength (Fig. 1). The breadth of the pass-band and the sharpness (roll-off rate) of the spectral lobes are determined by the bandwidth b. It follows that these parameters control the

temporal/spatial scale to be isolated and the degree of frequency/wavenumber localization. The aspect ratio determines the shape of the lobes and the spatial extend over which to smooth: for γ=1 the lobes are circular while contracting (dilating) the aspect ratio dilates (contracts) the spectral lobes in the radial direction. It is easy to see that the rotation of the filter shifts the peak frequency. Let $f_{\max}^{\theta}$ be the *peak frequency* at the angle θ. In the example of Fig. 1, if the sampling rate is 1s, then for θ=20° $f_{\max}^{20}$ = 0.13Hz, while for θ=50° $f_{\max}^{50}$ =0.0936Hz. It follows that in order for the peak to remain focused (tuned) on a given target frequency $f_{\max}^{\odot}$, one must adjust the length of the wavelet so that $f_{\max}^{\theta} \rightarrow f_{\max}^{\odot}$. Fig. 2 shows an example of tuning the filter at a given frequency. The same procedure is followed for tuning the filter at a given target wavenumber.

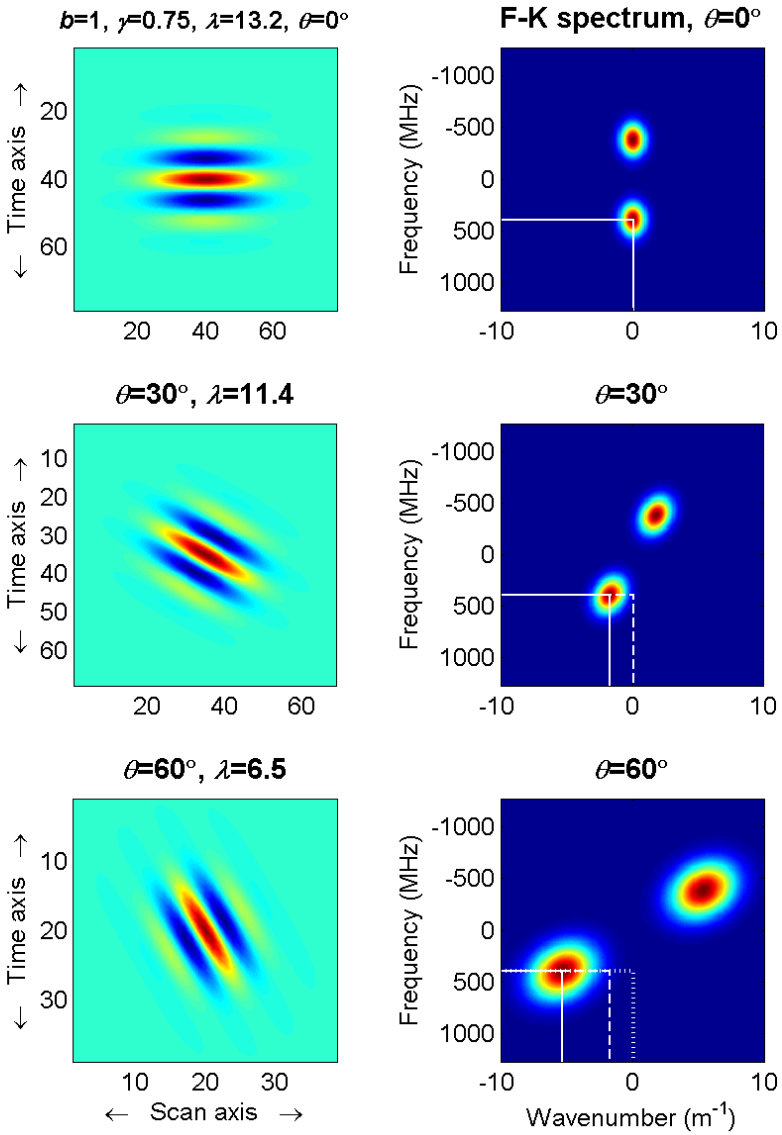

Figure 2. Tuning a Gabor Filter at a given target frequency (scale). Assume a radargram of size 512 samples × 512 traces, obtained with a 400MHz antenna, sampling rate of 0.1957 ns and a trace spacing of 0.025m. Let the invariant design parameters be γ = 0.75, b=1 and ψ=0°. Also let the target frequency $f_{\max}^{\odot}$ be 400 MHz. For a Gabor filter at θ=0° this will be achieved when λ = 13.2 (top). At θ=30°, $f_{\max}^{30} \equiv f_{\max}^{\odot}$ ≈ 400MHz when λ = 11.4 (middle) and at θ=60°, when λ = 6.5 (bottom).

In the general case a radargram may contain reflections from variable-dip reflectors or multiple reflectors with different dips. A single-dip Gabor filter will extract only part of the dip-dependent information because it is highly selective. This is restrictive when one wishes to extract scale-dependent information over a range of dips, in which case a more sophisticated approach is needed. The application of directional filters to edge and contour detection often involves the combination of partial images obtained by the same filter rotated to different directions. The solution used herein borrows insight from these techniques, but with adaptations for GPR data. Let $\chi_\odot$ be the target frequency or wavenumber, **D** the f-k transform of the data and **F** the normalized f-k transform of the filter at angle θ and length L, so that $\mathbf{F}(\theta,L)=\mathbf{G}(\theta,L)\cdot\|\mathbf{G}(\theta,L)\|_\infty^{-1}$. The procedure entails application of the filter rotated to different angles under adaptive control so as to remain tuned at a given $\chi_\odot$; this yields a series m = 1,…M of orientation-dependent outputs $\hat{\mathbf{D}}_m(\theta_m,\chi_\odot)=\langle\mathbf{D},\mathbf{F}\{\theta_m,L_m\}\rangle$ which are stacked in the WLS sense to yield the final output

$\bar{\mathbf{D}}(\theta_1:\theta_m,\chi_\odot) = \sum_{m=1}^{M}\hat{\mathbf{D}}_m(\theta_m,\chi_\odot)w(\theta_m,\chi_\odot)\Big/\sum_{m=1}^{M}w(\theta_m,\chi_\odot)$.

The stacking weight is generally a function of the form

$w(\theta_m,\chi_\odot)=\left\|\hat{\mathbf{D}}(\theta_m,\chi_\odot)\right\|_n\cdot\|\mathbf{D}\|_n^{-1}$,

n = 1, 2 or ∞, which guarantees that the final output will not be disproportionally dominated by powerful spectral components; stacking also enhances the S/N ratio. This scheme facilitates the combination of several "partial" same-scale-and-dip outputs into an image that is scale-dependent and may account for variations of the angle of dip.

3 Second Generation Discrete Curvelet Transform (DCT)

A curvelet frame is a wave packet frame on $L^2(\mathbb{R}^2)$ based on a second dyadic decomposition which, in effect, comprises an extension of the isotropic MRA concept to include anisotropic scaling and directionality while maintaining rotational invariance. Consider a vector of time or/and space variables $\mathbf{x}=[x_1\ x_2]^T$ and a vector of frequency or/and wavenumber variables $\boldsymbol{\xi}=[\xi_1\ \xi_2]^T$. In Cartesian coordinates curvelets are obtained by parabolic dilation, rotation and translation of a specifically shaped (mother) function $\varphi_{j,0,0}(\mathbf{x})\leftrightarrow\Phi_{j,0,0}(\boldsymbol{\xi})$ and have the form

$\varphi_{j,l,k}(\mathbf{x})=2^{3j/4}\varphi_{j,0,0}\left(\mathbf{S}_{\theta_l}^T(\mathbf{x}-\mathbf{x}_\mathbf{k}^{j,l})\right)\leftrightarrow\Phi_{j,l,k}(\boldsymbol{\xi})=2^{-3j/4}\Phi_{j,0,0}(\mathbf{S}_{\theta_l}\xi)\cdot e^{-i\langle\mathbf{x}_\mathbf{k}^{j,l},\xi\rangle}$

where $\mathbf{S}_{\theta_l}=\left([1\ -\tan\theta_l]^T\quad[0\ 1]^T\right)$ is the *shear* matrix, $\tan\theta_l = l\cdot2^{\lfloor -j/2\rfloor}$, $l=-2^{\lfloor j/2\rfloor},\ldots 2^{\lfloor j/2\rfloor}-1$ is a set of equi-spaced *slopes*, $\lfloor.\rfloor$ denotes the floor function (integer part) and

$$\mathbf{x}_\mathbf{k}^{j,l}=\mathbf{S}_{\theta_l}^{-T}\begin{bmatrix}2^{-j}&0\\0&2^{-j/2}\end{bmatrix}\begin{bmatrix}k_1\\k_2\end{bmatrix}=\mathbf{S}_{\theta_l}^{-T}\mathbf{b}_\mathbf{k}^j,\qquad k_1,k_2\in\mathbb{Z}^2$$

represent the translation parameters. Accordingly, curvelets are indexed by their scale 2^{-j}, $j\in\mathbb{N}_0$, orientation θ_l and location $\mathbf{x}_k$.

In the ξ-domain the curvelets $\Phi_{j,l,k=0}(\boldsymbol{\xi})$ are constructs like those illustrated in Fig. 3a and are supported in parabolically scaled, sheared trapezoidal wedges bounded as $\left\{(\xi_1,\xi_2):2^j\le\xi_1\le2^{j+1},\ -2^{-j/2}\le\frac{\xi_2}{\xi_1}-\tan\theta_l\le2^{-j/2}\right\}$; when completed by symmetry with respect to the origin and rotation by ±π/2 radians they generate the concentric partitioning of the Fourier plane, whose geometry is shown in Fig. 3b. Examples of *x*-domain Cartesian curvelets are shown in Fig 3d; they are long and slender waveforms with length proportional to $2^{-j/2}$ and width proportional to 2^{-j} (parabolically scaled); they oscillate in their transverse direction and are low-pass in their longitudinal direction.

A *curvelet coefficient* comprises the inner product between a function $f(\mathbf{x})\in L^2(\mathbb{R}^2)$ and a

curvelet $\varphi_{j,l,k}$: $c(j,l,k) = \left\langle f, \varphi_{j,l,k} \right\rangle = \sum_{x_1,x_2} f(\mathbf{x})\overline{\varphi_{j,l,k}(\mathbf{x})}$. The collection of curvelet coefficients over j, l and k comprises the forward DCT. The inverse DCT is appropriately defined by the reconstruction formula $f(\mathbf{x}) = \sum_{j,l,k} c(j,l,k)\varphi_{j,l,k}(\mathbf{x})$.

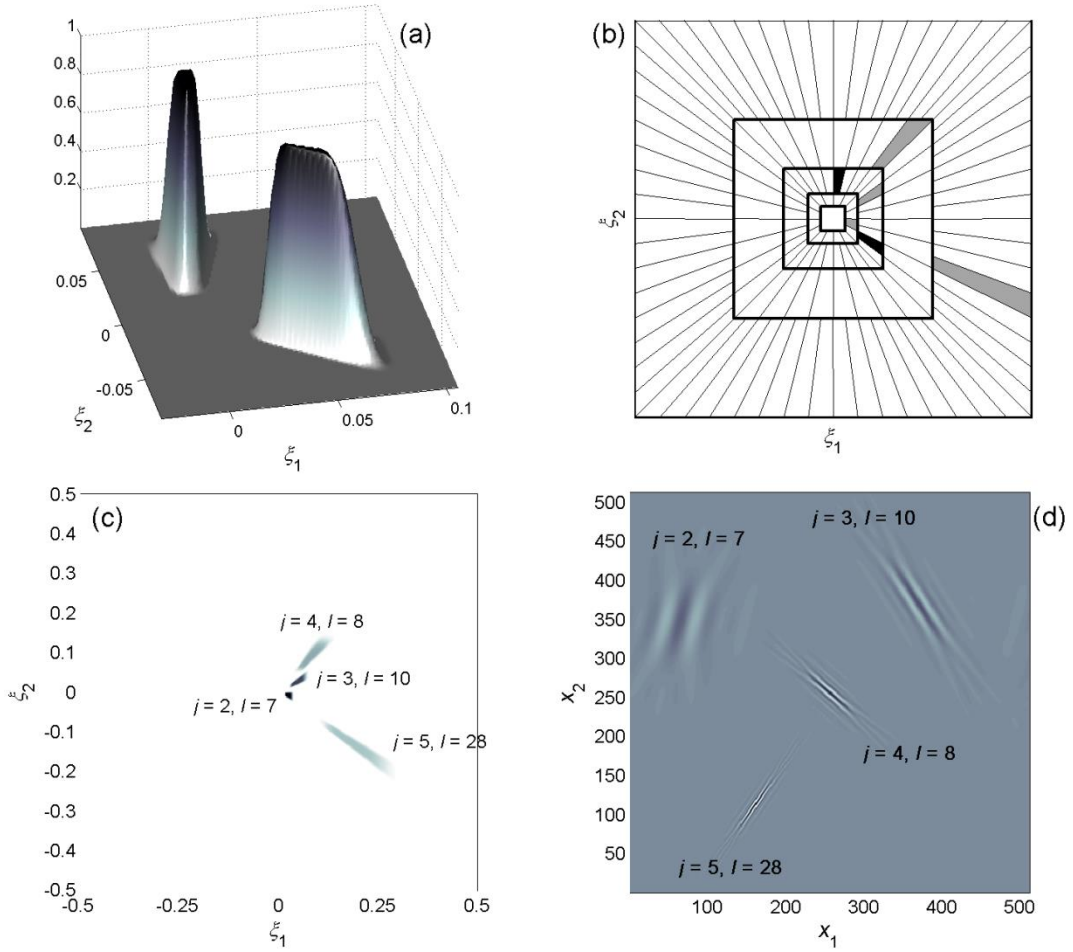

Figure 3. (a) Two examples of ξ-domain curvelets. **(b)** Illustrative example of the partitioning (tiling) of the ξ-plane in Cartesian coordinates with trapezoidal wedges. The pyramidal (scale) partitioning is based on N=6 scales. The inner (coarsest) scale corresponds to j = 1 and is isotropic because it cannot be partitioned with wedges. The angular partitioning begins at j=2 with $L_{j=2}$=16 wedges; the number of wedges doubles in every second scale. Each wedge supports a curvelet of a given scale (j) and slope (l). The angular indexing of the wedges (l) counts clockwise from the top-left corner of each scale. The finest-scale partition (j=6) is also isotropic and is not shown (see text). The solid black wedges at j=3, l=5 and j=3, l=15 indicate the right-hand side support of the curvelets shown in (a). The grey wedges indicate the supports of the curvelets shown in Fig. 3c, d. **(c)** Amplitudes of complex ξ-domain curvelets at different scales and orientations; the supports of these curvelets are shown grey-shaded in (b). **(d)** Arbitrarily translated x-domain curvelets, corresponding to the ξ-domain curvelets of (c).

Curvelets interact with curved objects $f(\mathbf{x})$ in three ways as shown in Fig. 4: (1) When curvelet and object intersect when aligned in their longitudinal directions, the transverse oscillatory part of the curvelet will locally match the same-scale component of the object the resulting coefficient will be significant. (2) When the curvelet and the object intersect at arbitrary angles information is lost to the curvelet's low-pass longitudinal action: the coefficients will have small amplitudes. (3) When the curvelet and the object do not intersect,

the coefficients will be near zero. Thus it is easy to see how one may use curvelets of appropriate scales and orientations to retrieve different traits of the data.

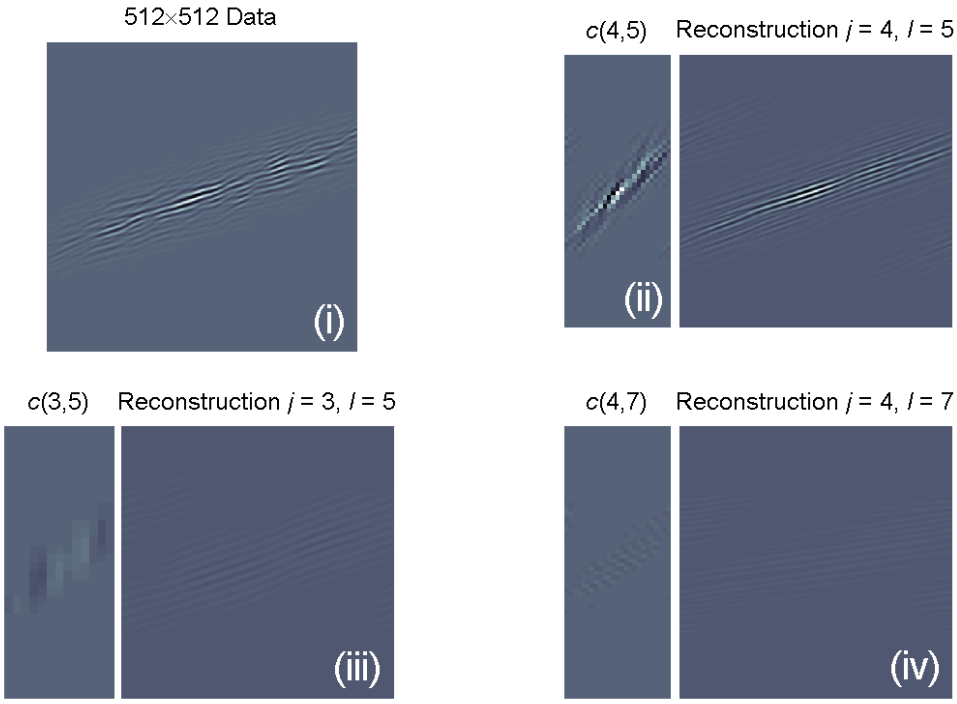

Figure 4. Demonstration of data and curvelet interactions: **(i)** The data comprises a 512×512 matrix with a set of uniformly up-dipping wavy reflections. **(ii)** The coefficients, (left) and a partial reconstruction of the data (right) generated by the curvelet {j = 4, l = 5}. This has a slope of –110°, perfectly aligned with the reflections, and extracts a strong component of the signal. **(iii)** As in (ii) but for {j = 4, l = 7}. The curvelet has a slope of –94° and intercepts the reflections at an angle of 14°; it cannot match signal of significant amplitude, hence coefficients and reconstruction are weak. **(iv)** As in (ii) and (iii) but for {j = 3, l = 5}. The curvelet has the right alignment but the wrong scale (weak coefficients).

In the applications shown herein, the DCT is computed with the "wrapping method" (Candès et al, 2006) found in the CurveLab software package (http://www.curvelet.org). The algorithm requires the number of scales N and the number of wedges $L_{j=2}$ at the second coarser scale (j = 2), at which the angular decomposition begins (L doubles in every second scale). The finest-level scale is associated with spectral content near the Nyquist. Because GPR data is typically oversampled, this usually consists of random noise; it is easier (and recommended) to assign wavelets instead of curvelets to that scale and treat it as isotropic. Once the DCT is computed, information can be manipulated by selecting coefficients according to their scale (j) and slope (l) and applying hard or soft thresholding; the data can then be totally or partially reconstructed by inverse DCT.

4 Examples

Two examples will be shown. The first illustrates the capability of multidirectional Gabor filtering and the CT to extract localized geometrical information at any scale or combination of scales. Figs. 6a and 7a illustrate a radargram collected with a Måla GPR system and 250MHz antenna at a levelled surface above massive fragmented limestone (Fig. 5). The data is shown after time-zero adjustment, global background removal and amplification with the "inverse amplitude decay" technique (e.g. Tzanis, 2010, p25). The dimensions of the data matrix are 1024 samples × 1340 traces (sampling rate of 0.1909ns, trace spacing 0.01996 m).

Noise is not a significant problem with the exception of some peculiar, interference of unknown origin, intermediate strength and "checkerboard" spatio-temporal characteristics appearing at different locations of the radargram. The main structural features are: (a) Down-dipping reflections attributed to synthetic fractures; examples of such reflections are marked with white arrows. (b) Very faint, up-dipping quasi-linear reflections attributed to antithetic fractures; these are marked with yellow arrows. Their apparent spatial widths can be measured on the radargram to 0.2 – 0.4 m, therefore their expected wavenumbers should be of the order of 2.5 – 5 m^{-1}. Their apparent azimuth can also be measured and ranges between –65° and –50°. (c) Clusters of strong reflections appearing along the traces of the fractures and mainly at their intersection, (e.g. between 5–10m and 40–80ns), corresponding to areas of intense fragmentation that are usually associated with filled karstic cavities.

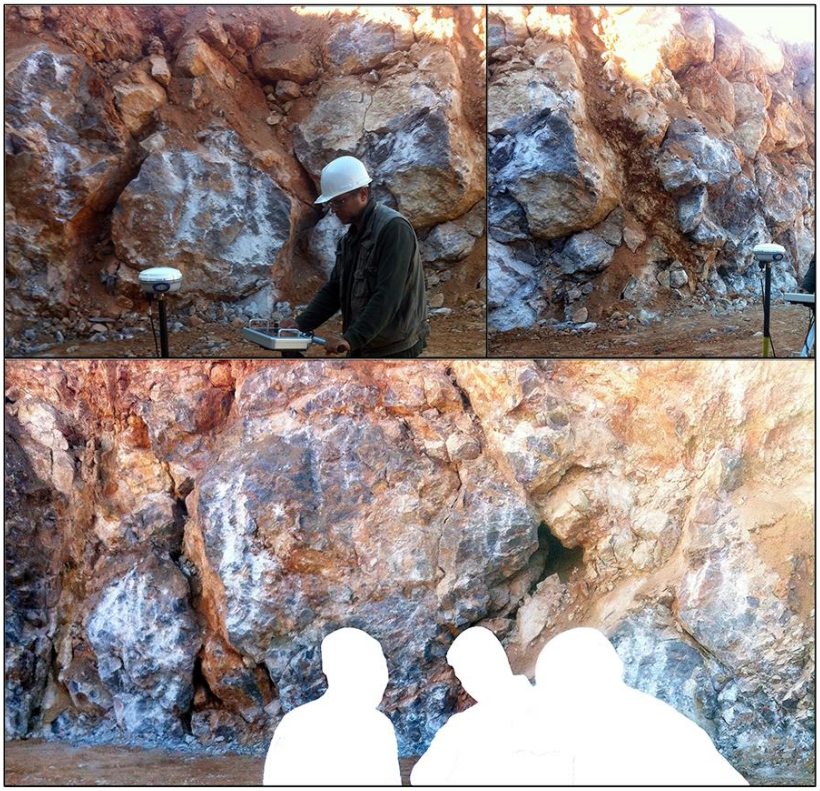

Figure 5. Geological setting in which the data of Example 1 were recorded. The subsurface comprises massive limestone, heavily fragmented due to conjugate normal faulting and jointing. Karstification has nucleated at the loci of faults and many of the voids and gaps were subsequently filled with lateritic material. All photographs are courtesy of Mr P. Sotiropoulos, Terra-Marine Ltd., Greece (http://terra-marine.gr).

Fig. 6 illustrates a (multi-directional) application of the Gabor. The expected wavenumbers associated with the up-dipping reflections indicates the design parameters: the target wavenumber was set to $k = 0.3m^{-1}$ and spatio-temporal localization was moderate so as to admit the entire expected range ($b = 1.5$). The aspect ratio was set to $\gamma = 0.5$ so as to favour linear features. Moreover, the range of expected dips defines the arc over which to apply the filter. Fig. 6b illustrates the output of a multidirectional application over the arc [115°, 130°] in steps of 5°. It is straightforward to see that albeit very weak and practically obscured by other data components, the up-dipping reflections of the antithetic fractures have generally been successfully detected. Fig. 6c illustrates the output of the same filter over the arcs [50°, 65°] $\cup$ [115°, 130°], so as to isolate reflections from both synthetic and antithetic fractures. In both cases fractures are detected at locations at which it was previously not possible, as for instance between distances 5 – 10 m and traveltimes 80 – 150 ns. Moreover, the relative

importance of synthetic and antithetic fractures becomes evident: the former have larger apertures and are filled with reflective material, thus generating stronger reflections and indicating that when they were active, they were the main carriers of local deformation.

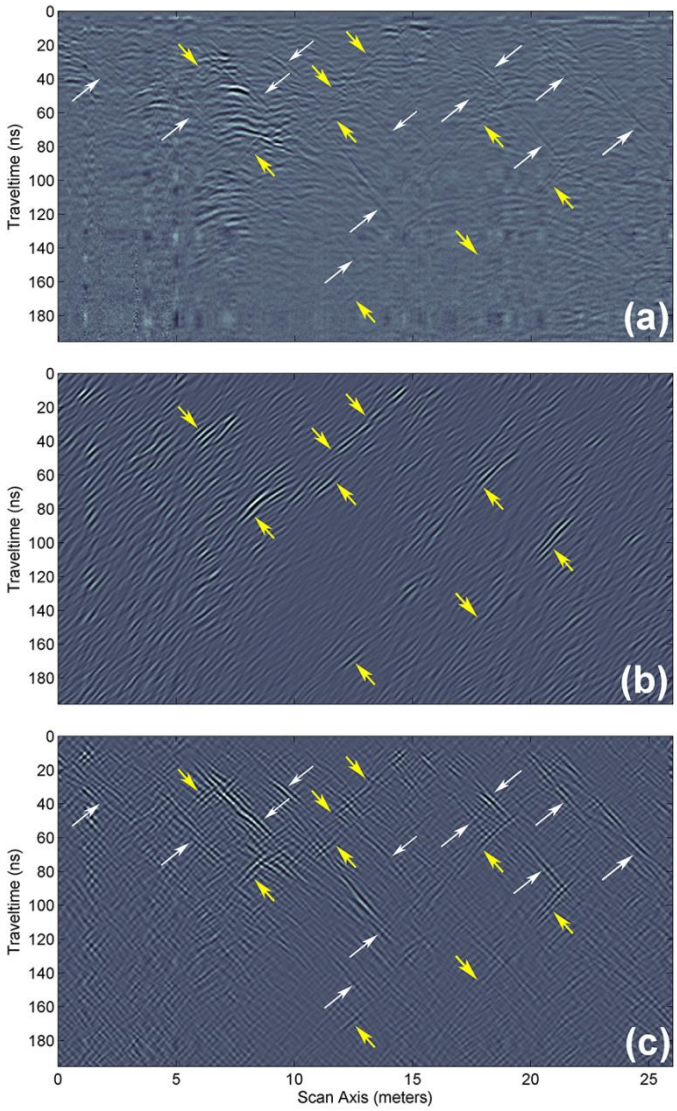

Figure 6. **(a)** Radargram collected with a Måla GPR system and 250MHz antenna at a levelled surface above massive fragmented limestone (Fig. 5). The white and yellow arrows point at faint down and up dipping reflections from synthetic (main) and antithetic fractures. The data was collected in association with Terra-Marine Ltd., Greece (http://terra-marine.gr) and is used courtesy of Mr. P. Sotiropoulos. **(b)** Reflections from antithetic fractures isolated by multidirectional application of a Gabor filter tuned at $k = 0.3\text{m}^{-1}$ over the arc [115°, 130°]. **(c)** Reflections from synthetic and antithetic fractures isolated by multidirectional application of the same filter over the arcs [50°, 65°] ∪ [115°, 130°].

The corresponding application of the Curvelet Filter is illustrated in Fig. 7. The complexity and fine texture of the targets (fractures) indicates that the curvelet decomposition should also be fine and was set to comprise 7 scales and 40 angles at the second coarser ($j = 2$) scale. In such a scheme, the up-dipping reflections belong to the 4^{th} ($2.07\ \text{m}^{-1} < k < 4.18\ \text{m}^{-1}$) and 5^{th} ($4.18\ \text{m}^{-1} < k < 8.33\ \text{m}^{-1}$) scales. Accordingly, the reconstruction was based only on these two scales and only on curvelets supported on wedges with slopes 112° – 133°, (normal and sub-normal to the apparent dip of the reflections). The remaining coefficients were shrunk to zero

(hard-thresholded). The results are shown in Fig. 7b. As scrutiny may show, the reconstruction successfully recovers the reflections of the antithetic fractures which can now be identified, mapped and analyzed easier. Fig. 7c shows a partial reconstruction of the data based on scales four and five and slopes [112°, 133°] ∪ [48°, 66]°; this is counterpart to Fig. 6c and isolates reflections from both the synthetic and antithetic fractures since the second set of slopes is (sub)normal to the apparent dip of the synthetic fractures. As previously, information about both sets of reflections is successfully recovered.

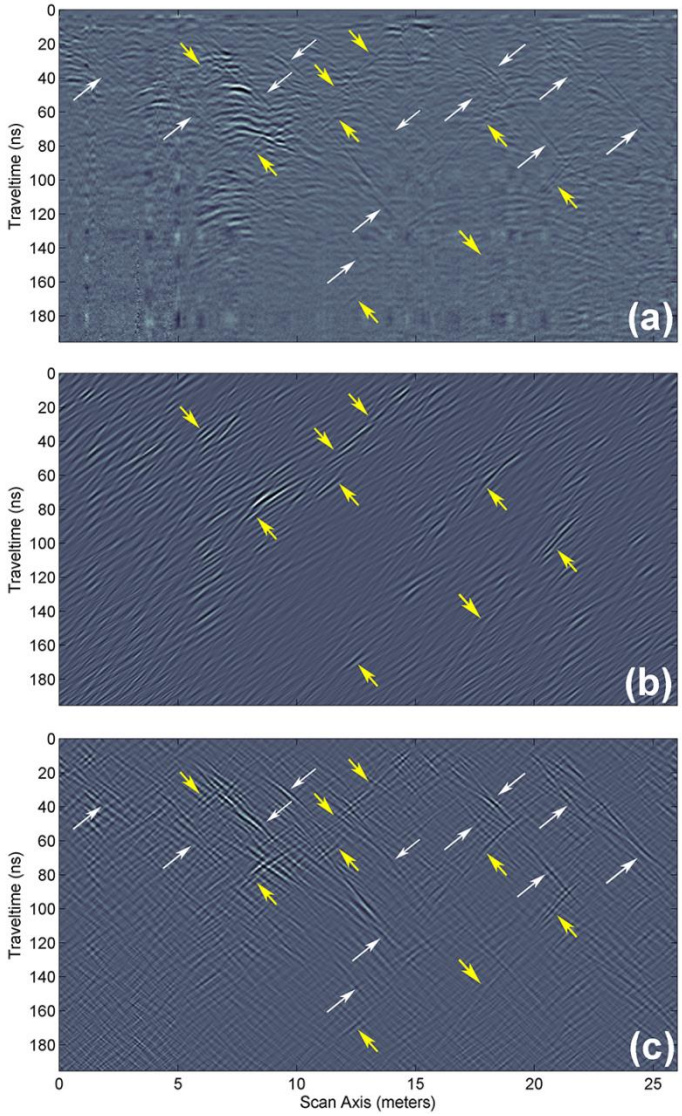

Figure 7. (a) As per Fig. 6a. The pyramidal decomposition of this data comprised seven scales and the angular decomposition began with 40 angles (wedges) at the second coarser scale. **(b)** Reflections from antithetic fractures isolated by and partial reconstruction from the coefficients {j = 4, j=5, $\theta_l \in$ [112°, 133°]}. **(c)** Reflections from synthetic and antithetic fractures isolated by partial reconstruction from the coefficients {j = 4, j=5, $\theta_l \in$ [112°, 133°] ∪ [48°, 66°]}.

The second example illustrates the de-noising power of multidirectional Gabor filtering and the CT. Fig. 8a illustrates a data set collected over ground consisting of thick, generally moist Holocene alluvial sediments with a significant argillaceous component, including a shallow (< 10m) unconfined aquifer. The surface was flat but rough, significantly vegetated and littered with small scatterers such as rocks and occasional metallic objects. The data was collected with a GSSI SIR-2000 system and Subecho-40 antenna (central frequency 40MHz)

and is shown after minimal pre-processing (global background removal). The dimensions of the data matrix are 512 samples × 2048 traces (sampling rate of 0.5889ns, trace spacing 0.02 m). The data is contaminated by severe, high-angle, high-wavenumber (> $2m^{-1}$) crossing clutter, random noise, reverberation from shallow scatterers (e.g. at distances 6m, 24.9m, 25.5m, 35m etc.). The noise is overwhelming at distances ca. 15m and 25–32m and everywhere at traveltimes > 180ns, obscuring the principal reflection from the aquifer (between 150–200ns) and any other information.

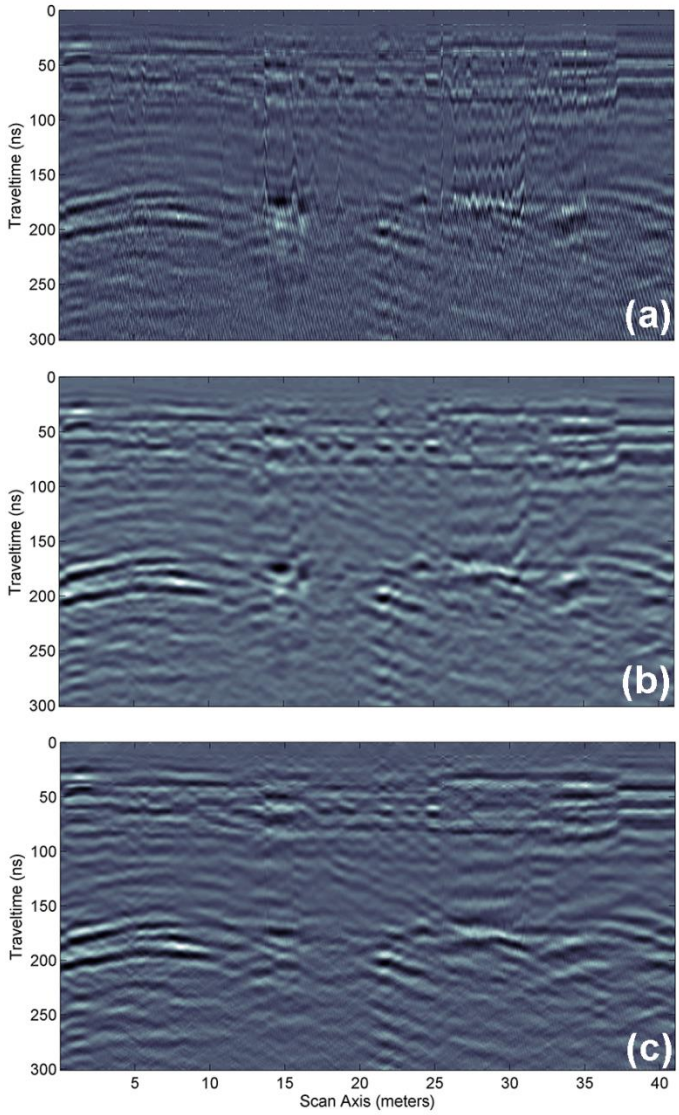

Figure 8. (a) Noisy data collected with a GSSI SIR-2000 system and Subecho-40 antenna over moist Holocene alluvial sediments; the main structural features comprise reflection(s) from an unconfined aquifer at travel times 150–250ns. **(b)** Noise-free data after multidirectional application of a Gabor filter (see text for details). **(c)** Noise-free data after curvelet decomposition and partial reconstruction (see text for details).

Fig. 8b shows the output of a multidirectional Gabor filter. Inasmuch as the noise is associated with wavenumbers > $2m^{-1}$ and there's no natural high frequency content in the data, the filter was tuned at $k = 1.75m^{-1}$ and applied over the arc [10°, 170°] in steps of 10°; the localization characteristics were somewhat relaxed so as to avoid severe narrow band-passing action ($b = 2$; $\gamma = 0.75$). The result is an almost faithful reproduction of the large-scale

data components and complete elimination of the clutter with particular reference to traveltimes > 150ns.

Fig. 8c shows the corresponding application of the curvelet filter. The data was decomposed into 6 scales (the highest permissible for the size of the time axis). The aspect ratio of the data matrix requires fine angular partitioning so as to obtain a sufficiently detailed representation of the shallow-dipping or sub-horizontal wavefronts that make up most of the useful data. Accordingly, the angular decomposition started with 40 angles at the second coarser (j = 2) scale. The output shown in Fig. 8c comprises a partial reconstruction based on coefficients of scales and slopes $\{j = 2, \theta_l \in [-22°, 22°]\} \cup \{j = 3, \theta_l \in [-60°, 60°]\} \cup \{j = 4, \theta_l \in [-60°, 60°]\} \cup \{j = 5, \theta_l \in [-66°, 66°] \setminus [-17°, 17°]\}$. The remaining coefficients were shrunk to 15% their original amplitude (soft-thresholded). The result is a faithful reproduction of the data less the noise and some larger scale, steeply dipping (> |60°|) features, as for instance the one seen at the distance of 30m and traveltimes 100–200ns. Scrutiny will show that these are the only practical differences between the outputs of the Curvelet and Gabor filters, with the latter performing slightly better in this case.

5 Conclusions

This work introduces the application of scale and orientation sensitive filtering methods to signal enhancement and geometric information retrieval from 2-D GPR data. These are a multi-directional adaptation of directional filtering techniques based on the 2-D Gabor wavelet and the Curvelet Transform which formulates an optimally sparse representation in terms of a pyramidal multiscale/multidirectional decomposition into highly anisotropic and localized elements. Both techniques are simple to use and very powerful, given that they can extract information about any recoverable trait of the data, sometimes with surgical precision. Notably, the CT has optimal reconstruction properties meaning that any *recoverable* piece of information can be retrieved from a noisy data set as if it was noise-free.

In general, these methods make it possible to:

a) Suppress directional noise wavefronts of any scale and angle of emergence in such an adaptive way, as not to interfere with any part of recoverable data components.
b) Retrieve waveforms of specific scale and geometry for further scrutiny, as for instance distinguish signals from small and large aperture fractures and faults, different phases of fracturing and faulting, bedding etc.

Although there is no objective metric to quantitatively assess their relative performance (since they are very different in design) their results are very comparable at least in terms of similitude in their outputs and where the degree of similitude is a matter of common sense. It is also obvious that applications are not limited to GPR!

Both types of filter are easy to automate for routine operation. However, they are more than "black boxes" since their real power rests on their exceptional adaptivity (within, of course, the limitations associated with the f-k transform on which the filters operate). Manual operation with some trial and error experimentation may come up with elaborate filtering schemes that frequently allow "surgical" operations on the data (with particular reference to the CT).

Plentiful additional information exists in the cited reference and also in Tzanis (2013), Tzanis (2014) and the extensive documentation accompanying the matGPR software (which also includes interactive MATLAB™ implementations and is currently available in http://users.uoa.gr/~atzanis/matgpr/matgpr.html). The later references include discussion of the inevitable caveats, which were not mentioned herein for shortage of space.

References

Candès, E., 1999. Harmonic analysis of neural networks. Appl. Comput. Harmon. Anal., 6, 197-218.

Candès, E. and Donoho, D., 2003a. Continuous curvelet transform: I. Resolution of the wavefront set. Appl. Comput. Harmon. Anal., 19, 162-197.

Candès, E. and Donoho, D., 2003b. Continuous curvelet transform: II. Discretization and frames. Appl. Comput. Harmon. Anal., 19, 198-222.

Candès, E. and Donoho, D., 2004. New tight frames of curvelets and optimal representations of objects with piecewise C^2 singularities. Comm. Pure Appl. Math., 57, 219-266.

Candès, E. J., L. Demanet, D. L. Donoho, and L. Ying, 2006. Fast discrete curvelet transforms (FDCT). Multiscale Modeling and Simulation, 5, 861–899.

Chui, C.K., 1992. An introduction to wavelets, Academic Press, New York.

Daugman, J.G., 1985. Uncertainty relations for resolution in space, spatial frequency, and orientation optimized by two-dimensional visual cortical filters. J. Opt. Soc. Am., 2, 1160-1169.

Feichtinger, H.G. and Strohmer, T, 1998. Gabor Analysis and Algorithms, Birkhäuser; ISBN 0817639594

Feichtinger, H.G. and Strohmer, T., 2003. Advances in Gabor Analysis, Birkhäuser; ISBN 0817642390

Jacques, L., Duval, L., Chaux, C. and Peyré, G., 2011. A panorama on multiscale geometric representations, interwining spatial, directional and frequency selectivity, Signal Processing, 91, 2699-2730; doi:10.1016/j.sigpro.2011.04.025

Kruizinga, P. and Petkov, N., 1999. Non-linear operator for oriented texture. IEEE Trans. Image Process., 8 (10), 1395-1407.

Grigorescu, C.E., Petkov, N. and Kruizinga, P., 2002. Comparison of texture features based on Gabor filters. IEEE Trans. Image Process., 11 (10), 1160-1167.

Mallat, S. and Peyré, G., 2007. A review of bandlet methods for geometrical image representation, Numer. Algorithms, 44 (3), 205-234.

Smith, H. F., 1998. A Hardy space for Fourier integral operators, J. Geom. Analysis, 7, 629 – 653.

Tzanis, A., 2010. matGPR Release 2: A freeware MATLAB® package for the analysis & interpretation of common and single offset GPR data, FastTimes, 15 (1), 17 – 43.

Tzanis, A, 2013. Detection and extraction of orientation-and-scale-dependent information from two-dimensional GPR data with tuneable directional wavelet filters. Journal of Applied Geophysics, 89, 48-67. DOI: 10.1016/j.jappgeo.2012.11.007

Tzanis, A, 2014. The curvelet transform in the analysis of 2-D GPR data: Signal enhancement and extraction of orientation-and-scale-dependent information. Journal of Applied Geophysics (in revision).